1-1-2014

Effect of niobium clustering and precipitation on strength of a NbTi-microalloyed ferritic steel

Andrii Kostryzhev
University of Wollongong, andrii@uow.edu.au

Abdullah Alshahrani
University of Wollongong, amfa065@uowmail.edu.au

Chen Zhu
The University of Sydney, czhu@uow.edu.au

Julie Cairney
The University of Sydney

Simon Peter Ringer
The University of Sydney

See next page for additional authors

Effect of niobium clustering and precipitation on strength of a NbTi-microalloyed ferritic steel

Abstract

The microstructure-property relationship of an NbTi-microalloyed ferritic steel was studied as a function of thermo-mechanical schedule using Gleeble 3500 simulator, optical and scanning electron microscope, and atom probe tomography.

Keywords

nbti, strength, precipitation, microalloyed, clustering, effect, ferritic, steel, niobium

Publication Details

Kostryzhev, A., Al-Shahrani, A., Zhu, C., Cairney, J., Ringer, S. P., Killmore, C. & Pereloma, E. V. (2014). Effect of niobium clustering and precipitation on strength of a NbTi-microalloyed ferritic steel. Material Science and Engineering A, 607 (June), 226-235.

Authors

Andrii Kostryzhev, Abdullah Alshahrani, Chen Zhu, Julie Cairney, Simon Peter Ringer, Chris Killmore, and E V. Pereloma

Effect of niobium clustering and precipitation on strength of a NbTi-microalloyed ferritic steel

A.G. Kostryzhev[1*], A. Al Shahrani[1], C. Zhu[2,3], J.M. Cairney[2,3], S.P. Ringer[2,3], C.R. Killmore[4], E.V. Pereloma[1,5]
[1]School of Mechanical, Materials and Mechatronic Engineering, University of Wollongong, NSW 2500, Australia
[2]Australian Centre for Microscopy and Microanalysis, The University of Sydney, NSW 2006, Australia;
[3]School of Aerospace, Mechanical and Mechatronic Engineering, The University of Sydney, NSW 2006, Australia;
[4]BlueScope Steel Limited, Five Islands Rd, Port Kembla, NSW 2505, Australia
[5]UOW Electron Microscopy Centre, University of Wollongong, NSW 2519, Australia

(C. Zhu is now with Tata Steel Research and Development, Swinden Technology Centre, Rotherham, S60 3AR, UK)

*corresponding author, email: kostryzhev@yahoo.com

Abstract

The microstructure-property relationship for a NbTi-microalloyed ferritic steel was studied as a function of thermo-mechanical schedule using a Gleeble 3500 simulator, optical and scanning electron microscopy, and atom probe tomography. Contributions to the yield stress from grain size, solid solution, work hardening, particle and cluster strengthening were calculated using the established equations and the measured microstructural parameters. With a decrease in the austenite deformation temperature the yield stress decreased, following a decrease in the number density of > 20 nm Nb-rich particles and ≈ 5 nm Nb-C clusters, although the grain refinement contribution increased. To achieve the maximum cluster/precipitation strengthening in ferrite, the austenite deformation should be carried out in the recrystallisation temperature region where there is a limited tendency for strain-induced precipitation. Based on the analysis of cluster strengthening increment, it could be suggested that the mechanism of dislocation-cluster interaction is closer to shearing than looping.

Keywords: microalloyed steel, thermo-mechanical processing, mechanical properties, electron microscopy, atom probe tomography

Introduction

The high strength low alloy (HSLA) steels are widely used in construction, oil and gas transportation, and production of heavy machinery, and cover approximately 12 % of the world steel production. Due to high loading in service, the requirements to steel strength and toughness are high, which are achieved by the careful selection of steel composition (in particular by additions of Nb, Ti, V, Mo) and the microstructure conditioning during processing [1-6]. The strengthening effect of Nb microalloying on steels occurs mainly via three microstructural mechanisms: ferrite grain refinement due to austenite grain boundary pinning, retardation of recrystallisation, and precipitation strengthening. Earlier research has shown that an increase in the Nb content leads to an increase in steel strength [7-10], and, in particular, the precipitation strengthening increment to the yield stress [11 - 18] (Table 1). When the strengthening increment is attributed to the Ashby-Orowan type mechanism, where dislocations bow between spherical-shaped obstacles, the strengthening increment may be considered as directly proportional to the square root of precipitate volume fraction, and inversely proportional to the precipitate diameter [10]. This offers a considerable range in the extent of possible strengthening via Nb precipitate dispersions, since the precipitate size and number density depend on the steel composition and the thermo-mechanical processing (TMP) parameters [3, 19-21]. As can be seen from Table 1, for the same steel composition the precipitation strengthening increment may vary by 4.5 times (from 20 MPa to 180 MPa [14]) following a variation in the TMP schedule. In particular, the strengthening increment increased with a decrease in coiling temperature [13] and with an increase in cooling rate [15]. Normalising in the austenite temperature region (about 900 C°) usually led to a decrease in the precipitation strengthening increment due to particle coarsening [11, 18]. The strengthening increment was observed increasing with Ti additions [11]. However, formation of coarse TiNb(C,N) particles may lead to the retardation of precipitation of fine Nb(C,N) particles [6, 22-24] and a decrease in the precipitation strengthening effect. The relative influence of Nb precipitation in the austenite versus precipitation in the ferrite on strengthening has been addressed [16]; although the study did not result in a clear conclusion as to whether the austenite or ferrite precipitation is more effective. Here we investigated this problem for a NbTi-microalloyed steel: (i) the Nb precipitation kinetics in austenite and ferrite (studied recently for this steel [25]) was modified via a variation in deformation temperature during TMP; (ii) the contributions to yield stress were estimated using empirical relationships and measured microstructural parameters (ferrite grain size, NbTi-rich precipitate size distribution and number density, Nb-C solute atom cluster dispersion, and ferrite matrix composition). The relative

influence of the microstructural parameters, in particular the Nb-C atom clustering, on strength is discussed.

Material and Experimental Techniques

A NbTi-microalloyed steel of composition 0.081C, 1.20Mn, 0.27Si, 0.021Ni, 0.019Cr, 0.1Mo, 0.016Cu, 0.037Al, 0.064Nb, 0.021Ti, 0.003V, 0.001S, 0.012P, and 0.0047N (wt. %) was provided by BlueScope Steel Ltd. Samples of size 10x15x20 mm were cut from the quarter-thickness position of a 230 mm thick continuously cast slab for TMP simulations. The TMP was carried out using a Gleeble 3500 thermo-mechanical simulator. Six TMP schedules were studied (Figure 1). The process involved the following steps:

- heating at 5 $C°s^{-1}$ heating rate to 1250 °C and holding at this temperature for 300 s,
- cooling to 1100 °C at 1 $C°s^{-1}$ cooling rate,
- a single hit of roughing deformation to 0.35 strain at 1100 °C at 5 s^{-1} strain rate,
- cooling to 1075 °C, 975 °C or 825 °C at 1 $C°s^{-1}$ cooling rate,
- a single hit of finishing deformation to 0.75 strain at 1075 °C, 975 °C or 825 °C at 5 s^{-1} strain rate;
- cooling to 800 °C (which is above the austenite to ferrite transformation temperature, $A_3 \approx 775$ °C, [26]) at 1 $C°s^{-1}$ cooling rate and water quenching to room temperature, or cooling to 600 °C (which is below A_3) at 1 $C°s^{-1}$ cooling rate, holding for 300 s, and then air-cooling to room temperature.

The three finishing deformation temperatures of 1075 °C, 975 °C and 825 °C were chosen because they are respectively above, near and below the recrystallisation stop temperature ($T_{nr} \approx 975$ °C [26]). Hereafter, the conditions corresponding to those samples quenched from 800 °C are designated as 1075-800, 975-800 and 825-800, whereas those samples studied after holding at 600 °C are designated as 1075-600, 975-600 and 825-600. Microstructural investigations of the TMP samples were conducted on samples cut parallel to the plain-compression plane (ND-CD plane).

Optical microscopy was carried out by using a Leica DMRM microscope equipped with Leica Application Suite (LAS) 4.0.0 image processing software. For the determination of the ferrite grain size distributions, 800-1000 grains were imaged from the mid-thickness position of each TMP sample. Measurements of the average grain size were carried out using Leica Grain Expert software.

Electron microscopy of NbTi-rich precipitates for the six TMP conditions was carried out by using JEOL 7001F FEG scanning electron microscope (SEM) operating at 5 kV. SEM sample preparation included polishing with diamond suspensions and slight etching with 2% Nital. For the determination

of particle size distributions and number density values, 60 - 270 particles (depending on TMP condition) were measured. The energy dispersive X-ray spectroscopy (EDS) semi-quantitative point analysis of NbTi-rich precipitates was carried out using an AZtec 2.0 Oxford SEM EDS system. For the determination of particle compositions 20 - 25 particles were analysed for each TMP condition.

Three samples after the 600 °C hold were investigated using Atom Probe Tomography (APT). A standard two-stage electropolishing technique [27] was used for the preparation of APT samples. The data collection was carried out using a Cameca Local Electrode Atom Probe (LEAP™), operating at a temperature of 20 K and a pulse fraction rate of 20% [28]. Volumes free of visible solute atom segregation were selected for determination of the matrix composition, after background noise subtraction. The maximum separation envelope method [29] was used for evaluation of the Nb-C clustering, using a value of d_{max} = 1 nm and N_{min} = 20. The Guinier radii, r_G, of clusters/fine precipitates were calculated from radii of gyration, l_g, data using the equation $r_G = \sqrt{5/3} \cdot l_g$ [29].

Vickers microhardness was measured for the three 600 °C hold TMP conditions using a Struers DuraScan testing machine with 0.1 kg load.

Results

Optical microscopy of low temperature microstructures

The microstructure of the steel after holding at 600 °C and slow cooling consisted of ferrite and pearlite (Figure 2). The average ferrite grain size decreased with a decrease in the finishing deformation temperature from 13 ± 8 μm for 1075-600 to 11 ± 7 μm for 975-600 and to 9 ± 4 μm for 825-600 TMP schedule. The second phase (pearlite) content was measured to be at a level of 4 - 5 % for all three 600 °C hold TMP conditions.

SEM study of precipitates

SEM revealed the presence of precipitates with diameters ranging between 20 – 170 nm for all six TMP conditions (Figure. 3). The average precipitate diameter, number density and chemistry varied with the deformation temperature and cooling conditions. The analysis of precipitate chemistry (Figure 4) and diameter distributions (Figure 5) resulted in separation of all the particles into two size groups: > 70 nm size and < 70 nm size. Particles in the > 70 nm size range were cuboidal (TiNb)(C,N), ellipsoidal Nb(C,N) or ellipsoidal NbC (Figures 4a - c). Particles in the < 70 nm size range were mainly spherical NbC (Figure 4d). After all studied TMP schedules, all particles in the < 70 nm size group were Ti free. The particle

size, morphology and chemistry observed in this work correspond to those reported for similar steel compositions [17, 30-33]. In the low temperature austenite (Table 2):

- a maximum of the > 70 nm particle number density and volume fraction was observed for the 975 – 800 schedule;
- a maximum of the < 70 nm particle number density and volume fraction was observed for the 825 – 800 schedule;
- the maximum amount of Nb(C,N) / NbC particles in the > 70 nm size group was observed for the 975 – 800 schedule;

In the ferrite (Table 2):

- a maximum of the particle number density and volume fraction in both size groups was observed for the 975 - 600 schedule;
- the maximum amount of Nb(C,N) / NbC particles in the > 70 nm size group was observed for the 975 – 600 schedule.

With a decrease in the deformation temperature a variation in the particle volume fraction between ferrite and austenite decreased, i.e. the number of particles that precipitated during the austenite to ferrite transformation and in ferrite decreased with a decrease in the deformation temperature.

APT study of atom clusters

The APT study revealed the presence of Nb-containing solute atom clusters and very fine precipitates with diameters in the range of 3 - 13 nm (Figure 6, Table 3). The chemical composition of these clusters varied with their size such that larger clusters contained less Nb. The Nb-C cluster / fine precipitate number density decreased with a decrease in the deformation temperature. The analysis of matrix composition revealed a slight increase in the C content in solid solution with a decrease in the deformation temperature (Table 4).

Mechanical properties

The ferrite microhardness was measured to be 197±14 VHN for the 1075 – 600, 186±13 VHN for the 975 – 600 and 174±7 VHN for the 825 – 600 schedule. To transform the hardness values into the corresponding yield stress values, a correlation equation, YS = 2.4 x HV, was determined in this work by using a linear approximation of the published data (Figure 7). In each literature source used [30, 34-36], the microhardness and the yield stress had both been measured and the steel chemistries, ferrite-pearlite microstructures and processing conditions were similar to those in this work. The microhardness

- yield stress correlation coefficient obtained here (2.4) is within the range of values (2.4 – 2.7) reported previously for other steel grades and processing conditions [20, 37-40]. Using the measured microhardness values, the average yield stress, σ_y, was calculated to be 473±34, 446±31 and 417±17 MPa for the 1075 – 600, 975 – 600 and 825 – 600 schedules, respectively.

Discussion

Development of Nb precipitation diagram

In the present work a Nb time-temperature-precipitation (TTP) diagram for the X70 steel was required to understand the influence of the TMP schedule on precipitation. Although a number of diagrams have been published in the literature, a diagram was not available for the steel composition and strain levels studied here. Therefore, the TTP diagram was obtained for the present work by using a linear approximation of the published data for similar steel compositions (Figure 8). The diagram determination was carried out in the following way: (i) equilibrium precipitation start and finish temperatures of Nb(C,N) were assumed to be 1100 °C and 800 °C respectively according to [41-44]; (ii) the first approximation of Nb(C,N) precipitation diagram was drawn on the bases of [45-47] for a steel containing 0.08C-0.064Nb-0.0047N deformed to 0.33 strain; (iii) due to the strain increasing the dislocation density and enhancing precipitation, a time step based on [41, 48, 49] in the direction of shorter times was applied to the TTP diagram after (ii) to reflect a higher strain (0.75) experienced by our steel; (iv) due to presence of Ti retarding Nb precipitation, following a decrease in free N and Nb and precipitation of TiN or TiNb-rich complexes, a time step based on [22, 23] in the direction of longer times was applied to the TTP diagram after (iii) to reflect presence of 0.021 wt.% Ti in our steel.

Influence of TMP schedule on Nb precipitation kinetics

In the analysis of the influence of TMP on Nb precipitation the following assumptions were made (Figure 9): (i) the precipitation of Nb(C,N) starts when the time-temperature curve of the TMP schedule crosses 1100 °C; (ii) the 1075 °C temperature of finishing deformation is too high to initiate strain-induced precipitation, due to quick annihilation of dislocations; and (iii) strain-induced precipitation starts after the finishing deformation at 975 °C or 825 °C, according to the TMP schedule.

As the cooling rate is similar for all schedules, the time available for precipitation in austenite is similar (about 200 s from the point of crossing the start C-curve of TTP diagram for non-deformed condition to 800 °C, Figure 9). However, the particle parameters varied with the deformation temperature (Table 2),

which is related to the variation in precipitation kinetics after straining. Thus, at the 1075 – 800 schedule strain-induced precipitation did not occur, which corresponds to a minimum of the Nb-rich particle total number density and volume fraction in austenite. The maximum time period available for strain-induced precipitation (about 175 sec, Figure 9) occurred for the 975 – 800 schedule. However, this sample had the lowest particle number density and volume fraction of < 70 nm particles, and the highest number density and volume fraction of > 70 nm particles. Obviously, the existing particles were growing at a greater rate, due to enhanced Nb diffusion, than new particles were precipitating. For the 825 – 800 schedule, the time of strain-induced precipitation was shorter (about 25 sec, Figure 9), compared to that for the 975 – 800 schedule, and the diffusion and dislocation annihilation were slower due to a lower processing temperature, compared to that for the 975 – 800 schedule. Therefore for particles > 70 nm, the number density and volume fraction were lower than those for the 975 – 800 schedule; and the < 70 nm particle number density and volume fraction were greatest for the 825 – 800 schedule.

After holding in ferrite (about 500 s compared to the 800 °C TMP schedules) both the particle number density and volume fraction increased for all three schedules due to a longer total precipitation time. However, the precipitation kinetics in ferrite varied with the deformation temperature in austenite. The highest particle number density and volume fraction in both size ranges occurred after the 975 – 600 schedule due to a longer time for strain-induced precipitation. However, a variation in the particle number density and volume fraction between ferrite and austenite (i.e. the number of particles precipitating in ferrite) was observed to be higher for the 1075 – 600 schedule. This can be explained by the following: for the 1075 – 600 schedule the precipitation in austenite proceeded according to the TTP diagram for non-deformed condition and progressed slowly during cooling; this resulted in a higher Nb content remaining in the matrix after the austenite to ferrite transformation; consequently, a higher amount of Nb precipitated in ferrite (compared to other schedules where strain-induced precipitation occurred).

Estimates of microstructural contributions to yield stress

Using the measured microstructural parameters and established empirical equations, we have sought to estimate the various microstructural contributions to strength. We have considered the influence of grain size, solid solution strengthening, clustering, precipitation and work hardening. These are now presented in turn.

The relationship between the average ferrite grain size, d, and the grain size strengthening increment, σ_{gs}, can be quantified using the Hall – Petch equation:

$$\sigma_{gs} = \sigma_0 + k \cdot d^{-1/2} \quad , \qquad (1)$$

The lattice friction stress, σ_0, may vary by up to 4.5 times, mainly due to the presence of solid solution strengthening elements (in particular free carbon), and was reported being in the range of 15 - 70 MPa [10, 50-53]. The grain size strengthening coefficient, k, insignificantly (up to 9 %) varies with steel composition, temperature and strain rate, and was reported being in the range of 21.4 – 23.5 MPa·mm$^{1/2}$ [10, 50-53]. In the present work σ_0 = 15 MPa and k = 21.4 MPa·mm$^{1/2}$ were accepted for pure iron [53], due to the carbon content and dislocation density being low in the studied steel and the effect of solid solution strengthening being calculated using a separate equation. Such an application of the Hall-Petch equation allowed to evaluate only the influence of ferrite matrix grains. The grain size strengthening contribution to the yield stress was calculated to be 204, 220 and 240 MPa for the 1075 – 600, 975 – 600 and 825 – 600 schedules, respectively (Table 5). The grain refinement contribution to the yield stress increased with a decrease in the deformation temperature due to the corresponding decrease in the average ferrite grain size. A possible increment to the yield stress from the pearlite was neglected due to the low measured amount of this phase (4 - 5 %).

The solid solution strengthening from Mn and Si can be estimated from the following empirical relationship [10]:

$$\Delta\sigma_{ss} = 83 \cdot C_{Si} + 32 \cdot C_{Mn} \, , \qquad (2)$$

where C_{Si} and C_{Mn} are Si and Mn contents (wt. %) in the ferrite matrix respectively. The matrix contents of Si in wt. %, as calculated from the APT data in at. %, were 0.25, 0.28 and 0.27 wt. % for the 1075 – 600, 975 – 600 and 825 – 600 schedules, respectively. The Mn content was calculated to be 0.73, 0.48 and 0.61 wt. % for the 1075 – 600, 975 – 600 and 825 – 600 schedules, respectively. This translates to a solid solution strengthening increment of 44, 39 and 42 MPa for the 1075 – 600, 975 – 600 and 825 – 600 schedules, respectively (Table 5).

Precipitation strengthening from the precipitates was estimated using the Ashby-Orowan equation [10], which assumes that dislocations cannot penetrate the obstacles, but rather loop around them:

$$\Delta\sigma_{ps} = \frac{10.8\sqrt{f}}{D} \ln\left(\frac{D}{6.125 \cdot 10^{-4}}\right) \qquad (3)$$

where f is the particle volume fraction and D is the particle diameter in μm.

Values for the precipitate dispersions, as measured using SEM imaging (Table 2), were used to estimate the following values of precipitation strengthening increment: for the < 70 nm particles – 51, 62 and 45 MPa for the 1075 – 600, 975 – 600 and 825 – 600 schedules, respectively; and for the > 70 nm particles – 28, 28 and 24 MPa for the 1075 – 600, 975 – 600 and 825 – 600 schedules, respectively (Table 5). A

variation in the yield stress contribution from the NbTi-rich particles followed a variation in the particle number densities (Table 2).

The work hardening contribution to the yield stress can be estimated using the long range work-hardening theory [54]:

$$\Delta\sigma_{wh} = \frac{\alpha}{2\pi} Gb\sqrt{\rho} \qquad (4)$$

where $\alpha = 0.5$ is a constant, G = 85000 MPa is the shear modulus, b = 0.286 nm is the Burgers vector and ρ is the dislocation density. The dislocation density was not measured in this work. However, an analysis of the literature for similar steel compositions and processing parameters [55-59] suggested a dislocation density of about $1 \cdot 10^{14}$ m^{-2} in the studied steel. Based on this value, the work hardening increment to the yield stress was estimated to be 19 MPa for all three 600 °C hold TMP conditions.

The cluster strengthening increment to the yield stress, $\Delta\sigma_{cl}$, can be estimated via subtraction of the grain size, solid solution, particle strengthening and work hardening contributions from the measured yield stress:

$$\Delta\sigma_{cl} = \sigma_y - (\sigma_{gs} + \Delta\sigma_{ss} + \Delta\sigma_{ps} + \Delta\sigma_{wh}). \qquad (5)$$

Substitution of the previously estimated contributions into equation (5) gives the cluster strengthening increment of 127, 78 and 47 MPa for the 1075 – 600, 975 – 600 and 825 – 600 schedules, respectively.

With an increase in the deformation temperature the measured microhardness (yield strength) increased, although the grain refinement contribution to the yield stress decreased following an increase in the grain size. This trend in microhardness (yield strength) can be attributed to an increase in the precipitation strengthening and cluster strengthening increments, which follow an increase in the amount of precipitation in ferrite with an increase in the deformation temperature. The precipitation strengthening increment observed in this work (70 – 90 MPa) corresponds to the earlier reported data for steels with ferrite-pearlite (Table 1), ferrite-bainite (73 MPa [60]) and ferrite/bainite/martensite (57 – 98 MPa [61]) microstructures. The cluster strengthening effect observed in this work (47 – 127 MPa) corresponds to the earlier reported data for steels with ferrite/bainite/martensite microstructures (24 – 100 MPa [61]); however, it was lower than that in a 0.08 wt. % Nb microalloyed steel with a fully bainitic microstructure (165 MPa [62]). This can be explained by a lower number of potential dislocation-cluster interaction sites in the steel studied here compared to [62]: (i) the presence of Ti in the steel studied here led to formation of coarse TiNb(C,N) particles which reduced the Nb content in the matrix available for atom clustering and, together with a lower Nb content in the steel studied here

(0.06 wt. %), resulted in > 10 times lower cluster number density than in [62] (< 60 x 10^{-6} nm^{-3} here vs 715 x 10^{-6} nm^{-3} in [62]); and (ii) the dislocation density in the slowly cooled ferrite-pearlite microstructure studied here (10^{14} m^{-2}) is about 10 times lower than the dislocation density which might be expected in a quickly cooled fully bainitic microstructure (10^{15} m^{-2} [63]) studied in [62].

Calculation of cluster strengthening increment

This work and related literature [61, 62] indicate that the relative potency of Nb solute atom clusters and nanoscale precipitates as strengthening agents is high, although the mechanism of dislocation-cluster interactions leading to this strengthening potency is still not fully understood and requires a separate investigation. The analysis of our APT data did not show any obvious crystallographic arrangement of the atoms in the Nb-C clusters, and a variable Fe-Nb-C composition (Figure 6, d). Here we have chosen to estimate the strengthening effect from the Nb-C solute atom clusters assuming the dislocation-cluster interaction mechanism being: (i) shearing of coherent precipitates possessing crystallographic arrangement of atoms (the calculation carried out using the order strengthening relationship); and (ii) looping around incoherent precipitates (the calculation carried out using the Ashby-Orowan equation).

The order strengthening relationship was used in the following form [64]:

$$\Delta\sigma_{c1} = 0.81 \cdot M \cdot \frac{\gamma}{2b} \cdot \left(\frac{3\pi f}{8}\right)^{0.5} . \qquad (6)$$

Here, M = 2 is the matrix orientation factor, b = 0.286 nm is Burgers vector, γ is the matrix-cluster interface energy and f is the cluster volume fraction. The interfacial energy was calculated previously to be 0.5-1.5 Jm^{-2} for the Fe – C interface [65], ~3 Jm^{-2} for the Fe – Nb interface [65], and ~1 Jm^{-2} for the Fe – NbC interface [66]. For our Nb-C clusters enriched in carbon we assumed: γ = 1 Jm^{-2}.

For the Nb-C clusters (Table 3), the cluster strengthening increment calculated using equations (3), (5) and (6) is presented in Table 6. The cluster strengthening contribution decreased with a decrease in the deformation temperature following a decrease in the cluster number density. The values of cluster strengthening increment calculated using the selected models and the measured parameters of clusters are significantly higher than those predicted using the measured yield stress. This could be explained if: (i) the cluster number density was overestimated as a result of their non-uniform distribution and small volume of APT data analysis, and (ii) not all the clusters equally participated in the dislocation-cluster interaction process due to a reduced dislocation density. The values of cluster strengthening increment obtained for the assumption that the dislocation-cluster interaction mechanism resembles shearing of coherent precipitates showed the closest match to the values predicted using the measured yield stress.

This may indicate that the dislocation-cluster interaction mechanism resembles shearing, although atoms in the clusters do not form the same strength bonds as atoms in the crystal lattice of a precipitate. A more detailed investigation and the development of equations to describe the mechanism of dislocation-cluster interaction are required to support this suggestion.

Conclusions

This study of Nb precipitation, microstructure-property relationships and cluster strengthening in NbTi-microalloyed steel resulted in the following conclusions:

1. A maximum rate of Nb precipitation in austenite occurred at an intermediate deformation temperature (975 °C for the studied steel), which corresponds to the nose temperature of the time-temperature-precipitation diagram (C-curve) of Nb(C,N), due to the balance between the relatively high diffusion rate, and the relatively low dislocation annihilation rate.
2. With an increase in the austenite deformation temperature, the amount of precipitation in austenite decreased due to a decreased tendency for strain-induced precipitation as a result of an increase in both Nb solubility and dislocation annihilation rate. With an increase in the austenite deformation temperature the amount of precipitation in ferrite increased, due to a larger Nb content available in solution below the austenite to ferrite transformation temperature.
3. The precipitation strengthening increment was observed to be in the range of 47 – 127 MPa from ≈ 5 nm Nb-C clusters and in the range of 70 – 90 MPa from > 20 nm Nb-rich particles. To achieve a maximum strengthening in practice a thermo-mechanical processing schedule should prevent high temperature precipitation of Nb, and therefore should be individually correlated to the steel composition.
4. Analysis of the predicted values for the cluster strengthening increment suggests that the dislocation-cluster interaction mechanism resembles shearing. A development of the theory for cluster strengthening mechanism is required.

Acknowledgement

The authors are grateful to the Australian Research Council and BlueScope Steel (LP110100231) for financial support of the project, and to the AMMRF node at the University of Sydney (Sydney Microscopy & Microanalysis) for assistance with atom probe tomography. The authors are grateful to Dr M.K. Miller, ORNL for the provision of the program for cluster analysis. Scanning electron

microscopy was carried out using FEGSEM JSM 7001F microscope (LE0882813) at the Electron Microscopy Centre at the University of Wollongong.

References

1. J. Beynon, C.M. Sellars, ISIJ Int. 32 (3) (1992) 359-367.
2. P.D. Hodgson, R. K. Gibbs, ISIJ Int. 32 (12) (1992) 1329-1338.
3. W.P. Sun, M. Militzer, D.Q. Bai, J.J. Jonas, Acta Metall. Mater. 41 (12) (1993) 3595–3604.
4. A. J. DeArdo, Ironmak. Steelmak. 28 (2) (2001) 138-144.
5. A. J. DeArdo, R. Marraccini, M. J. Hua, C. I. Garcia, Mater. Sci. Forum. 539-543 (2007) 28-35.
6. M. Gomez, L. Rancel, S. Medina, Mater. Sci. Forum. 638-642 (2010) 3388-3393.
7. W.B. Morrison, Mater. Sci. Technol. 25 (9) (2009) 1066-1073.
8. J.M. Gray, Int. J. of Pres. Ves. and Pip. 2 (1974) 95-122.
9. A. J. DeArdo, Int. Mater. Rev. 48 (6) (2003) 371-402.
10. T. Gladman, The physical metallurgy of microalloyed steels, the Institute of Materials, Cambridge University Press, Cambridge, 1997.
11. H.-J. Kestenbach, S. S. Campos, E. V. Morales, Mater. Sci. Technol. 22 (6) (2006) 615-626.
12. J. Irvine, T.N. Baker, Mater. Sci. Eng. 64 (1984) 123-134.
13. M.A. Altuna, A. Iza-Mendia, I. Gutierrez, Metall. Mater. Trans. A 43 (12) (2012)4571-4586.
14. Y. Imai, Y. Shono, Nucl. Eng. Technol. 2 (4) (1970) 279 – 287.
15. H-J. Kestenbach, Mater. Sci. Technol. 13 (9) (1997) 731 – 739.
16. H.-J. Kestenbach, J. Gallego, Scripta Mater. 44 (2001) 791–796
17. R.D.K. Misra, K.K. Tenneti, G.C. Weatherly, G. Tither, Metall. Mater. Trans. A 34 (2003) 2341 – 2351.
18. M. Charleux, W.J.Poole, M. Militzer, A. Deschamps, Metall. Mater. Trans. A 32 (2001) 1635 - 1647.
19. E. Valdes, C.M. Sellars, Mater. Sci. Technol. 7 (1991) 622-630.
20. M. Gomez, P. Valles, S. F. Medina, Mater. Sci. Eng. A 528 (2011) 4761 – 4773.
21. S. F. Medina, A. Quispe, M. Gomez, Metall. Mater. Trans. A 45 (2014) 1524-1539.
22. A.C. Kneissl, P. Baldinger, J. Phys. IV, Suppl. J. Phys. III, 3 (1993) 77 – 82.
23. S. G. Hong, K.B. Kang, C.G. Park, Scripta Mater. 46 (2002) 163 – 168.
24. R. Wang, C. I. Garcia, M. Hua, K. Cho, H. Zhang, A. J. DeArdo, ISIJ Int. 46 (9) (2006) 1345-1353.
25. E.V. Pereloma, A.G. Kostryzhev, A. AlShahrani, C. Zhu, J. M. Cairney, C. R. Killmore and S.P. Ringer, Scripta Mater. 75 (2014) 74 – 77.
26. A. Al Shahrani, T. Schambron, A. Dehghan-Manshadi, J. Williams, E. Pereloma, Mater. Sci. Forum 654-656 (2010) 298 - 301.
27. Gault BG, Moody MP, Cairney JM, Ringer SP, Atom probe microscopy, Springer, New York, 2012.
28. L. Yao, J.M. Cairney, C. Zhu, S.P. Ringer, Ultramicroscopy, 111 (2011) 648-651.
29. M.K. Miller, Atom probe tomography: analysis at the atomic level, Springer, New York, 2000.
30. He Kejian,T. N. Baker, Mater. Sci. Eng. A 169 (1993) 53-65.
31. E.V. Pereloma, J.D. Boyd, Mater. Sci. Technol. 12 (1996) 808-817.
32. A.J. Craven, K. He, L.A. Garvie, T.N. Baker, Acta Mater. 48 (2000) 3857 – 3868.

33. E.V. Pereloma, B.R. Crawford, P.D. Hodgson, Mater. Sci. Eng. A 299 (2001) 27–37.
34. S.N. Prasad, D.S. Sarma, Mater. Sci. Eng. A 408 (2005) 53 – 63.
35. J.P. Ormandy, M. Strangwood, C.L. Davis, Mater. Sci. Technol. 19 (2003) 595 – 601.
36. A.G. Kostryzhev, M. Strangwood, C.L. Davis, Mater. Manuf. Processes 25 (1-3) (2010) 41 – 47.
37. E.J. Pavlina, C.J. Van Tyne, J. Mater. Eng. Perform. 17 (6) (2008) 888-893.
38. I.A. Yakubtsov, P. Poruks, J.D. Boyd, Mater. Sci. Eng. A 480 (2008) 109‑116.
39. W.K. Kim, H.G. Jung, G.T. Park, S.U. Koh, K.Y. Kim, Scripta Mater. 62 (2010) 195‑198.
40. S.H. Hashemi, Mater. Sci. Eng. A 528 (2011) 1648 – 1655.
41. Y. Zeng, W. Wang, J. Mater. Sci. 43 (2008) 874 - 882
42. B. Soenen, S. Jacobs and C. Klinkenberg, Proceedings of Materials Solutions Conference, 7 - 9 October 2002, Columbus, Ohio, USA, pp. 16 – 24.
43. A. Pandit, A. Murugaiyan, A. Saha Podder, A. Haldar, D. Bhattacharjee, S. Chandra, R.K. Ray, Scripta Mater. 53 (2005) 1309 – 1314.
44. H. Zou, Kinetics of carbonitride precipitation in microalloyed steels, PhD Thesis (1991) McMaster University, Canada, downloaded from: http://digitalcommons.mcmaster.ca/opendissertations/3580.
45. B. Dutta, C. M. Sellars, Mater. Sci. Technol. 3 (1987) 197 – 206.
46. B. Dutta, E.J. Palmiere,C. M. Sellars, Acta Mater. 49 (2001) 785 – 794.
47. Y. Xu, Y. Yu, X. Liu and G. Wang, J. Mater. Sci. Technol. 22 (2) (2006) 149 – 152.
48. S. Okaguchi, T. Hashimo, ISIJ Int. 32 (3) (1992) 283 – 290.
49. J.-S. Park, Y.-S. Ha, S.-J. Lee, Y.-K. Lee, Metall. Mater. Trans. A 40 (2009) 560 – 568.
50. A. Cracknell, N.J. Petch, Acta Metall. 3 (1955) 186 – 189.
51. B.W. Christ, G.V. Smith, Acta Metall. 15 (1967) 809 – 816.
52. N.J. Petch, Acta Metall. 12 (1964) 59 – 65.
53. D.J. Dingly, D. McLean, Acta Metall. 15 (1967) 885 – 901.
54. R.W. Cahn, Physical Metallurgy, North-Holland Publishing, Amsterdam, 1970.
55. H.G. Hillenbrand, M. Graf and C. Kalwa, Development and production of high strength pipeline steels, EUROPIPE, GmbH, www.europipe.de, 2001.
56. F. Yin, T. Hanamura, O. Umezawa, K. Nagai, Mater. Sci. Eng. A 354 (2003) 31 – 39.
57. T. Ono, Y. Tomota, P. Lukas, D. Lugovy, D. Neov, N. Tsuchida, K. Nagai, Mater. Sci. Technol. 20 (2004) 121 – 125.
58. H. Yu, Y. Kang, H. Dong, J. of Univ. Sci. Technol. B. 13 (5) (2006) 406 – 410.
59. A.G. Kostryzhev, M. Strangwood, C.L. Davis, Ironmak. Steelmak. 36 (3) (2009) 186 - 192.
60. I. Olivares, M. Alanis, R. Mendoza, B. Campillo, J. A. Juarez-Islas, Ironmak. Steelmak. 35 (6) (2008) 452 - 457
61. I. B. Timokhina, M. Enomoto, M.K. Miller, E.V. Pereloma, Metall. Mater. Trans. A 43 (7) (2012) 2473-2483.
62. K. Y. Xie, T. Zheng, J. M. Cairney, H. Kaul, J. G. Williams, F. J. Barbaro, C. R. Killmore, S. P. Ringer, Scripta Mater. 66 (2012) 710–713.
63. H.K.D.H. Bhadeshia, Bainite in steels: transformations, microstructure and properties, IOM Communications Ltd, London, 2001.
64. D. N. Seidman, E. A. Marquis, D. C. Dunand, Acta Mater. 50 (2002) 4021–4035.
65. H. Sawada, T. Ozaki, Nippon Steel Technical Report, 102 (2013), pp. 9 – 14.
66. D.H.R. Fors and G. Wahnström, Phys. Rev. B 82 (2010) paper 195410.

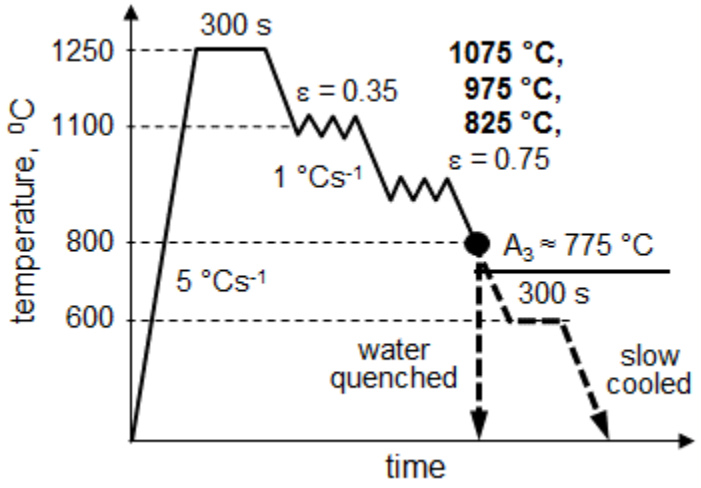

Figure 1. The schematic diagram of thermo-mechanical processing.

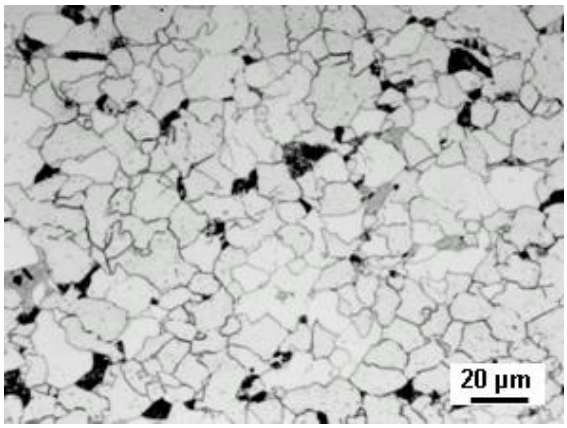

Figure 2 Representative optical image of the ferrite-pearlite microstructure in the studied steel (975 – 600 TMP schedule)

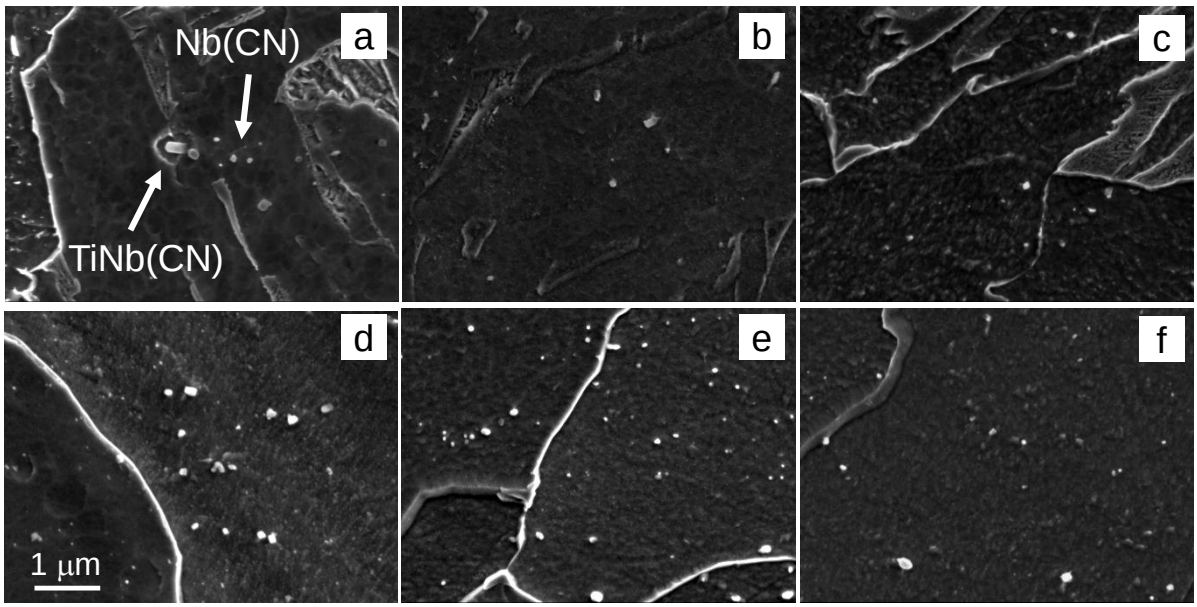

Figure 3. Representative SEM images of TiNb- and Nb-rich precipitates for the six studied TMP schedules: (a) 1075 – 800, (b) 975 – 800, (c) 825 – 800, (d) 1075 – 600, (e) 975 – 600, (f) 825 – 600.

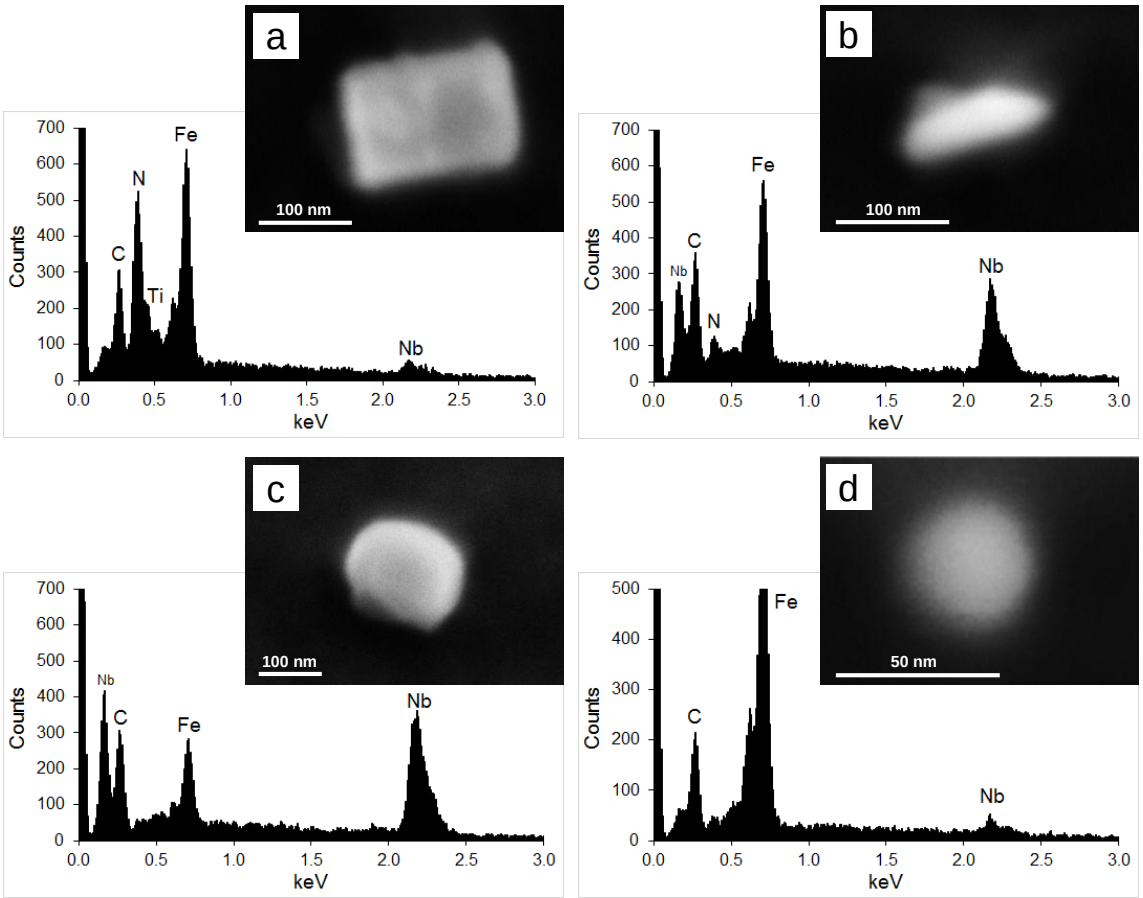

Figure 4. Typical SEM micrographs and corresponding EDS spectra of coarse (a) TiNb(CN), (b) Nb(CN), (c) NbC and (d) fine NbC particles.

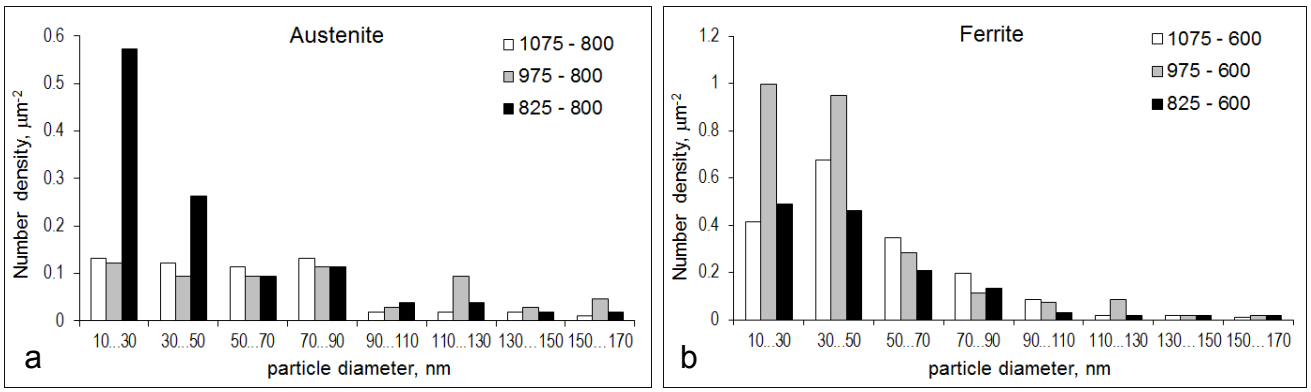

Figure 5. Nb-rich particle distributions in (a) austenite (samples quenched from 800 °C) and (b) ferrite (samples slow cooled after holding at 600 °C).

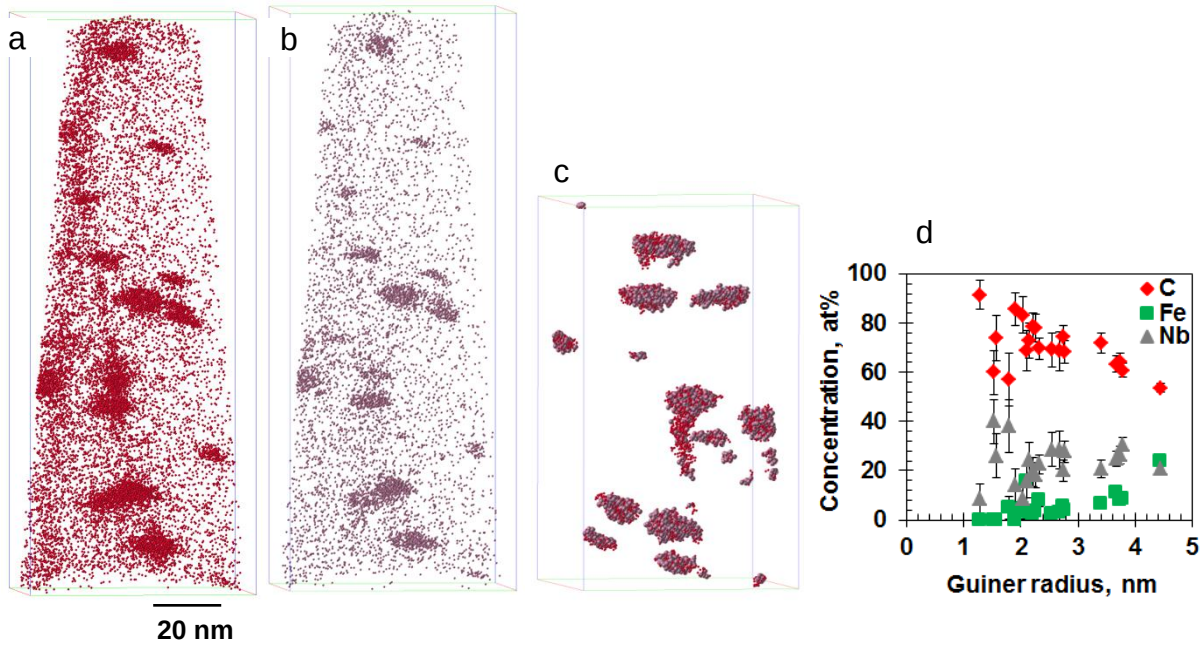

Figure 6. Representative (a) C and (b) Nb atom maps, (c) selected map of Nb-C clusters and (d) a variation in the cluster composition with cluster size (all for the 1075 – 600 TMP schedule).

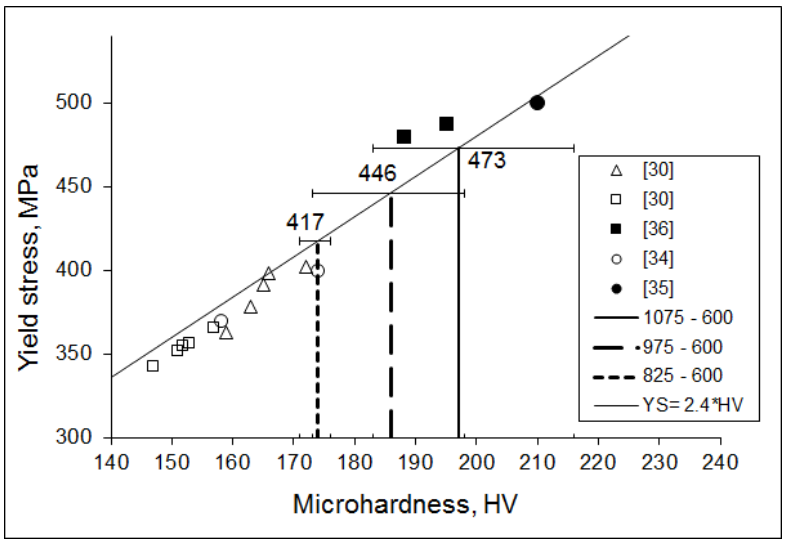

Figure 7. Determination of the HV microhardness – yield stress correlation equation for the studied steel and processing conditions using the literature data.

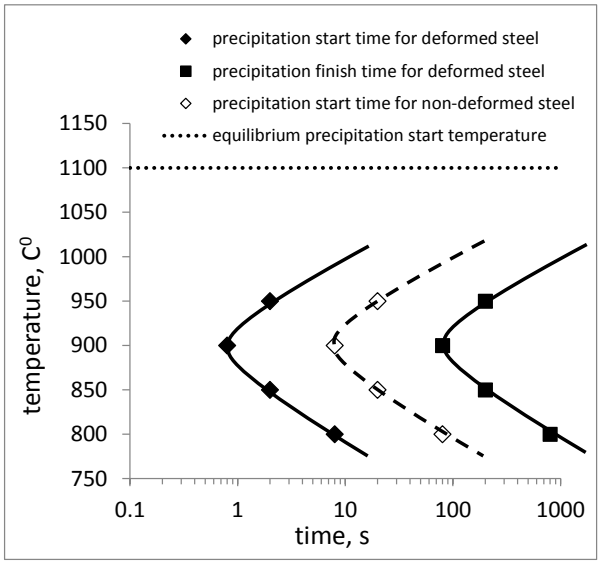

Figure 8. The estimated Nb(C,N) TTP diagram for the X70 steel (deformed condition is 0.75 strain).

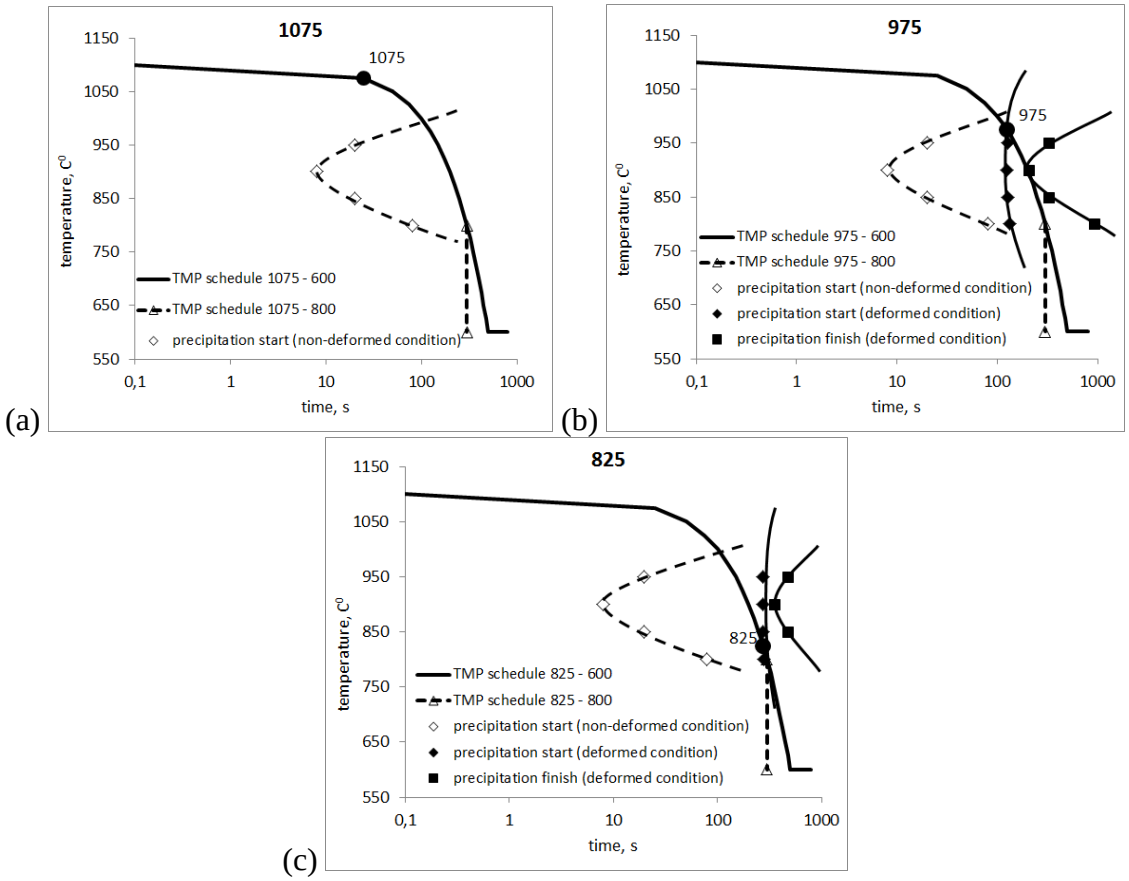

Figure 9 TMP processing schedule correlation to the Nb(C,N) TTP diagram for the (a) 1075 °C, (b) 975 °C and (c) 825 °C finishing deformation temperatures (zero time corresponds to the point of crossing 1100 °C during cooling, i.e. time when the TTP diagram for non-deformed condition starts; closed circles denote deformation temperatures and times, i.e. times when the TTP diagram of strain-induced precipitation starts)

Table 1. Increment to the yield stress from Nb microalloying in steels with ferrite-pearlite microstructure

Steel composition, wt %	Processing	ΔYS, MPa	Ref.
0.07 C – 0.04 Nb – 0.009N	Commercially hot rolled at 1080 – 890 °C	59	[11]
0.04 C – 0.064 Nb	Laboratory rolled below 1100 °C	40 - 85	[12]
0.06 C – 0.056 Nb – 0.0059N	Laboratory deformed at 1100 °C	60 - 180	[13]
0.20 C – 0.090 Nb – 0.005 N	Normalized at 925 – 1200 °C	20 - 180	[14]
0.023 C – 0.34 Nb - 0.0098 N	Forged at 1180 – 910 °C	71 - 210	[15]
0.12 C – 0.06 Nb – 0.05 Ti	Commercially hot rolled	65 - 112	[16]
0.052 C – 0.088 Nb – 0.047 Ti - 0.009 N	Normalized at 1000 – 1200 °C	40 - 180	[14]
0.06 C – 0.08 Nb – 0.07 Ti	Commercially rolled and coiled at 650 °C	190	[17]
0.07 C – 0.086 Nb – 0.047 Ti – 0.007N	Commercially rolled and coiled at 640 °C	230	[18]
0.11 C – 0.04 Nb – 0.008N - 0.11 Ti	Commercially hot rolled at 1045 – 895 °C	210	[11]

Table 2. Variation in the NbTi-rich particle parameters with TMP schedule

Finish processing temperature, °C		800 (austenite)					
Deformation temperature, °C		1075		975		825	
Particle size range, nm		< 70	>70	< 70	>70	< 70	>70
Chemistry, % of total amount	Nb(C,N) and NbC	100	29	100	77	100	20
	TiNb(C,N)	0	71	0	23	0	80
Number density, μm^{-2}		0.36	0.20	0.31	0.31	0.93	0.23
Average diameter, nm		41±15	93±15	41±16	117±25	31±12	109±25
Volume fraction*		0.0006	0.0012	0.0005	0.0036	0.0008	0.0023
		0.0018		0.0041		0.0031	
Finish processing temperature, °C		600 (ferrite)					
Chemistry, % of total amount	Nb(C,N) and NbC	100	33	100	75	100	20
	TiNb(C,N)	0	67	0	25	0	80
Number density, μm^{-2}		1.44	0.33	2.23	0.31	1.15	0.22
Average diameter, nm		41±12	98±17	34±12	110±20	35±12	103±25
Volume fraction*		0.0021	0.0026	0.0024	0.0031	0.0013	0.0019
		0.0047		0.0055		0.0032	
Variation in volume fraction between ferrite and austenite		0.0029		0.0014		0.0001	

* the area fraction of particles, measured using SEM imaging, can be assumed equal to the volume fraction of particles for the high number of particles studied in this work

Table 3. Variation in the Nb-rich cluster parameters with TMP schedule determined from APT data and calculated based on the number of atoms.

TMP schedule	C, at %	Nb, at %	Fe, at %	$r_{G,}$ nm	Number of atoms in cluster	Number density, $x10^{-6}$ nm^{-3}
1075-600	62.6±8.6	35±8.5	2.3±1.6	2.5±0.2	24-41	60
	64.7±3.9	24.4±3.7	10. 6±1.8	3.4±0.9	22-693	
	69.5±5.3	17.6±4.7	11.9±2.7	3.1±1.3	28-906	
975-600	50.9±9.3	46.0±9.3	3.1±2.5	1.9±0.3	24-35	50
	65.7±6.9	31.3±6.8	2.8±1.5	2.2±0.5	22-203	
	73.3±7.3	23.2±6.9	3.5±2.3	2.1±0.4	20-85	
	86.3±5.7	10.5±5.1	3.0±1.9	1.8±0.3	20-70	
825-600	59.4±6.8	35.6±6.7	4.5±2.9	2.0±0.8	26-79	34
	69.9±5.1	24.6±4.9	5.1±1.8	2.8±1.0	33-446	
	65.3±4.2	15.8±3.4	17.9±3.0	3.3±1.3	21-601	

Table 4. Variation in the ferrite matrix composition with TMP schedule determined from APT data and calculated based on the number of atoms (iron is balance).

	Element concentrations, at%										
	C	Al	V	Si	Mn	Mo	Cr	P	Cu	Nb	Ti
Nominal	0.374	0.076	0.003	0.534	1.213	0.058	0.02	0.022	0.014	0.038	0.024
1075-600	0.011 ±0.001	0.088 ±0.003	0.002 ±0.001	0.594 ±0.008	0.879 ±0.010	0.026 ±0.002	0.033 ±0.002	0.050 ±0.002	0.001 ±0.001	0.001 ±0.001	0.001 ±0.001
975-600	0.015 ±0.001	0.105 ±0.002	0.004 ±0.001	0.651 ±0.004	0.582 ±0.004	0.040 ±0.001	0.033 ±0.001	0.046 ±0.001	0.006 ±0.001	0.009 ±0.001	0.003 ±0.001
825-600	0.017 ±0.001	0.092 ±0.003	0.002 ±0.001	0.623 ±0.007	0.725 ±0.007	0.075 ±0.002	0.028 ±0.001	0.020 ±0.001	0.004 ±0.001	0.002 ±0.001	0.002 ±0.001

Table 5. Contributions to the yield stress calculated using the measured microstructural parameters and measured microhardness

TMP schedule	Calculated contributions to the yield stress, MPa						Measured hardness, HV	YS from HV, MPa
	grain size	solid solutes	precipitates		dislocations	clusters		
			<70 nm	>70 nm				
1075-600	204	44	51	28	19	127	197 ± 14	473 ± 34
975-600	220	39	62	28	19	78	186 ± 13	446 ± 31
825-600	240	42	45	24	19	47	174 ± 7	417 ± 17

Table 6. Values of the cluster strengthening increment calculated using various relationships, MPa

TMP schedule	Estimate from HV, Eq. 5	Shearing, Eq. 6	Looping, Eq. 3
1075-600	127	192	284
975-600	78	175	259
825-600	47	145	214